

Reservoir stimulation and induced seismicity: Roles of fluid pressure and thermal transients on reactivated fractured networks



Ghazal Izadi*, Derek Elsworth

Department of Energy and Mineral Engineering, EMS Energy Institute and G³ Center, Pennsylvania State University, University Park, PA 16802, USA

ARTICLE INFO

Article history:

Received 27 March 2013

Received in revised form 2 January 2014

Accepted 21 January 2014

Keywords:

Reservoir stimulation

Induced seismicity

Evolution of permeability in EGS reservoirs

Hydraulic and thermal transport in EGS reservoirs

ABSTRACT

We utilize a continuum model of reservoir behavior subject to coupled THMC (thermal, hydraulic, mechanical and chemical) processes to explore the evolution of stimulation-induced seismicity and related permeability in EGS reservoirs. Our continuum model is capable of accommodating changes in effective stresses that result due to the evolving spatial variations in fluid pressure as well as thermal stress and chemical effects. Discrete penny-shaped fractures (~10–1200 m) are seeded within the reservoir volume at both prescribed (large faults) and random (small fractures) orientations and with a Gaussian distribution of lengths and location. Failure is calculated from a continuum model using a Coulomb criterion for friction. Energy release magnitude is utilized to obtain the magnitude-moment relation for induced seismicity by location and with time. This model is applied to a single injector (stimulation) to the proposed Newberry EGS field (USA). Reservoir stimulation is assumed to be completed in four zones at depths of 2000, 2500, 2750 and 3000 m. The same network of large fractures (density of 0.003 m⁻¹ and spacing 300 m) is applied in all zones and supplemented by more closely spaced fractures with densities from 0.26 m⁻¹ (deepest zone) through 0.5 m⁻¹ (shallow zone) to 0.9 m⁻¹ (intermediate depth zone). We show that permeability enhancement is modulated by hydraulic, thermal, and chemical (THMC) processes and that permeability increases by an order of magnitude during stimulation at each depth. For the low density fracture networks, the increase in permeability reaches a smaller radius from the injection point and permeability evolution is slower with time compared to the behavior of the higher density fracture network. For seismic events that develop with the stimulation, event magnitude (M_s) varies from -2 to +1.9 and the largest event size (~1.9) corresponds to the largest fractures (~1200 m) within the reservoir. We illustrate that the model with the highest fracture density generates both the most and the largest seismic events ($M_s = 1.9$) within the 21 day stimulation. Rate of hydraulic and thermal transport has a considerable influence on the frequency, location and time of failure and ultimately event rate. Thus the event rate is highest when the fracture network has the largest density (0.9 m⁻¹) and is located at depth where the initial stresses are also highest. Also apparent from these data is that the closely spaced fracture network with the higher stress regime (at the deeper level) has the largest b -value ~0.74.

© 2014 Elsevier Ltd. All rights reserved.

1. Introduction

Stimulation of natural fractures provides a method to increase production in conventional geothermal wells and low permeability regions of otherwise productive geothermal systems. Effective stimulation is provided by circulating fluid through fractures and produces a permeable reservoir volume to extract heat energy from the rock mass. Injection induced pore pressure as well as thermal stresses may enhance the fracture networks and create conductive pathways (Elsworth, 1989a; Murphy, 1982; Nemat-Nasser, 1982; Pine and Cundall, 1985; Purcaru and Berckemer,

1978). For stimulation at stresses below the minimum principal stress, induced seismicity results by hydro-shearing of fracture zones through the reservoir for a variety of stress, temperature and geochemical regimes (Baisch et al., 2010; Bruce et al., 2009; Shapiro and Dinske, 2009a,b).

Early practice in this area has shown that the interaction of fluid pressures on fracture networks within a geothermal reservoir is one of the key technical challenges in reservoir stimulation (Renshaw, 1995; Shapiro et al., 1998; Zoback and Harjes, 1997). Seismic activity is a function of the fluid conductivity of the fracture distribution and the injection rate (Rutqvist et al., 2002; Shapiro and Dinske, 2007). For a given distribution of conductive fractures a limit for event magnitude can be determined as a function of flow rate and reservoir volume (Dinske et al., 2010; Evans et al., 2005; Shapiro et al., 1998). Models are typically classified by their

* Corresponding author. Tel.: +1 814 777 4099.

E-mail addresses: ghazal.izadi@gmail.com, gui2@psu.edu (G. Izadi).

conceptualization of the fractured reservoir geometry as either networks of discrete fractures or as equivalent porous media. In the following we use a continuum model of reservoir evolution subject to coupled THMC processes to explore the evolution of stimulation-induced seismicity and evolution of permeability in a prototypical EGS reservoir. We use the resulting fluid pressure and thermal stresses on rate, location and magnitude of seismic events in the short term.

In particular we define the relationship between the magnitudes of these induced seismic events and the applied fluid injection rates as well as the evolution of thermal stress. During stimulation of the single injection or production well we observe the enhancement of fracture permeability as a result of circulating fluid through these fracture networks under geothermal conditions. Together, hydraulic and thermal effects contribute to the reactivation of the natural fracture network and this may enhance the permeability. Both these effects may reactivate natural fractures and induce seismicity during stimulation. Our focus is to determine dominant behaviors controlling the enhancement of permeability and the triggering of induced seismicity that is unique in comparison to previous studies.

We then explore how pore-pressure and thermal stress can be linked to the seismic frequency-magnitude distribution, which is described by its slope, the *b-value*. We evaluate this response for the proposed stimulation of the Newberry EGS site and illustrate the modeled event-size distribution and evolution of related event-sizes due to fluid and thermal effects during a short-term (~21 days) proposed stimulation. We show that permeability enhancement is modulated by hydraulic, thermal, and chemical (THMC) (Taron and Elsworth, 2009) processes which also migrate through the reservoir on different length-scales and timescales (Elsworth and Yasuhara, 2010; Taron and Elsworth, 2009) and may also trigger seismicity.

2. Model description

Our objective is to determine the effect of hydraulic- and thermal-mechanical stimulation in the evolution of induced seismicity and of permeability during short term reservoir stimulation. Fracture networks provide a path for fluid transmission in a prototypical EGS reservoir. As fluid is circulated, changes in total stress result due to the penetration of fluid, the accompanying migration of fluid pressures, and as a result of thermal and chemical strains. These changes in the stress regime may drive portions of the reservoir toward failure with this failure accompanied by a seismic release of energy.

The THMC simulator (Taron et al., 2009), links FLAC^{3D} and TOUGHREACT by a separate code, referred to as the “interpolation

module”, capable of parsing data outputs from each primary simulator as input to the companion. In addition to data interpolation, the module executes constitutive relationships including permeability evolution response to stress, and thermodynamically controlled fluid compressibility. All flow and transport equations are derived from the principles of mass (or energy) conservation. The models for fluid have been discussed in detail by Pruess (1987) and Pruess et al. (1999). FLAC^{3D} is used for mechanical deformation, where undrained fluid allows calculation of the short-time build-up in fluid pressures that results from an instantaneous change in stress. The complex thermodynamics of phase equilibria of multiphase water mixtures can be tracked in the pre-existing framework of TOUGHREACT. The modeling structure calculates permeability change from the combined action of, thermo-mechanical, hydro-mechanical deformation, with each depending on temperature, effective stress, and chemical potential.

Chemical reactions are assumed to represent the geochemical systems. Component or primary species are defined and mass action equation is used for the rate of dissolution and participation of components. Kinetic rates are calculated within TOUGHREACT based on activation energy, rate constants at 25 °C, gas constant and absolute temperature.

We apply a coupled THMC model (Taron et al., 2009) with static-dynamic frictional strength-drop to determine energy release for fractures of small (10 m) to large (1200 m) diameter embedded within an elastic medium. The change of stress state is calculated from the pore pressures, thermal drawdown and chemical effects within FLAC^{3D}-TOUGHREACT (Taron and Elsworth, 2009). The model incorporates the effects of fractured reservoirs involving fracture networks of variable densities and connectivities and for various reservoir conditions of initial stress, temperature, and permeability – as these may exert significant influence on the evolution of permeability and seismicity.

We represent brittle failure on a pre-existing fracture as a prescribed stress drop (~3 MPa). For a prescribed frictional strength the model calculates the shear resistance from the change of normal stress and pore pressure. Stress builds and reaches a peak strength followed by a rapid decline to a residual strength (Goodman, 1976; Jaeger et al., 2007). This model is used to follow the evolution of seismic rupture within the system.

This model has been previously applied to two EGS reservoir fields (Izadi and Elsworth, 2013) and verified against these field data. This model is now applied to the doublet geometry (700 m spacing) within a larger reservoir geometry with half-symmetry (2000 m × 1000 m × 300 m) (Fig. 1) representative of the Newberry geothermal field. The Newberry demonstration EGS project is located southeast of Bend, Oregon. Data from well NWG 55-29 are used to build a reservoir model used in the subsequent

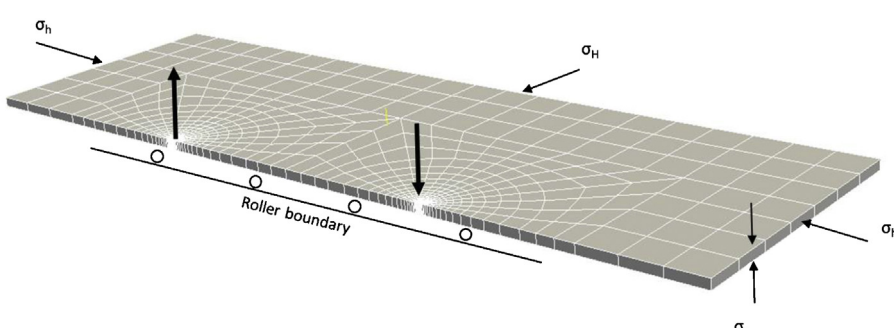


Fig. 1. Geometric layout of EGS reservoir as used in the simulation. Reservoir geometry with half-symmetry (2000 m × 1000 m × 300 m). The spacing between injection and production well is assumed 700 m. A vertical and two horizontal stresses are indicated.

Table 1
Solid medium properties as used in simulations.

| Parameter | Unit | Newberry |
|---|----------------|----------|
| Bulk modulus of intact rock (K_m) | GPa | 17 |
| Cohesion | MPa | 10 |
| Poisson's ratio (ν) | – | 0.27 |
| Bulk modulus of fluid (k_f) | GPa | 8 |
| Bulk modulus of solid grain (K_s) | GPa | 54.5 |
| Internal friction angle (ϕ) | ° | 35 |
| Residual friction angle (β) | ° | 11 |
| Coefficient of thermal expansion (α_T) | 1/°C | 1.2E–5 |
| Thermal conductivity (λ) | W/m K | 2.9 |
| Heat capacity (c_p) | J/kg K | 918 |
| Initial permeability (k) | m ² | 1.10E–17 |
| Porosity within fractures (ϕ) | – | 1.0 |

simulation (Cladouhos et al., 2011). This presumed half-symmetry is only approximate but represents the essence of important behaviors that act in the reservoir.

The present model applies the vertical stress as the lithostatic and two horizontal principal stresses, which are designated as the maximum and minimum principal stresses. During stimulation, fluid pressure is increased within the near-wellbore rock volume with low permeability, causing shear displacement of some of the existing fractures. This model calculates the flow rate, pressure and temperature distribution during stimulation. The changes in pressure and temperature induce displacements that consequently lead to a new change in pressure distribution.

In this study the modeling is considered for the reservoir defined as four different zones (shallow to deep) and at four different depths of 2000, 2500, 2750 and 3000 m. The four zones are defined from fracture structures (as zones B, C, D, and E) and with horizontal stresses increasing with depth as identified in Table 3. Boundary stresses, in both horizontal and vertical directions, pore pressure and temperatures corresponding to depths of 2000, 2500, 2750 and 3000 m are applied to the four different realizations of this geometry (Table 3) applied for this geothermal field. The characteristics and the values of the parameters utilized in simulation for the in situ reservoir are defined in Table 1. Each of these zones requires different inputs for fracture orientations and density as defined in Table 4. Reactive composition of the host reservoir rock is presented in Table 5. Calcite and amorphous silica are expected to be the minerals primarily responsible for permeability change due to precipitation and dissolution. Other likely minerals are also followed, as listed in Table 5. Rate constants for precipitation/dissolution and mineral reactive surface areas of these common minerals are available in the literature (Kovac et al., 2006; Xu and Pruess, 2001), and were utilized as in Xu and Pruess (2004).

2.1. Model dimensions and zones

The reservoir volume that is utilized in all models is the same for zones B, C, D and E (Fig. 1). For the Newberry EGS reservoir model the open hole is divided into five zones (A, B, C, D and E)

Table 3
Parameters utilized in the simulation.

| Parameters | Unit | Depth (m) | | | |
|-------------------------|------|----------------|----------------|----------------|----------------|
| | | 2000 Zone B | 2500 Zone C | 2750 Zone D | 3000 Zone E |
| $S_{h\min}$ | MPa | 36 | 45 | 50 | 54 |
| $S_{h\max}$ | MPa | 48 | 58 | 64 | 70 |
| S_v | MPa | 48 | 60 | 66 | 72 |
| $P_{\text{injection}}$ | MPa | 29 | 33 | 35 | 37 |
| $P_{\text{reservoir}}$ | MPa | 24 | 28 | 30 | 32 |
| $P_{\text{production}}$ | MPa | 19 | 23 | 25 | 27 |
| Peak strength | MPa | 25 | 30 | 35 | 38 |
| T_{rock} | °C | 230 | 280 | 290 | 310 |
| $T_{\text{injection}}$ | °C | 20 | 20 | 20 | 20 |

from BHTV (Borehole televIEWer) fracture density and lithology. Based on observation from the BHTV data, four zones (B, C, D and E) may be the best targets for stimulation. The characteristics of these zones are summarized in Table 2.

The moderate fracture density in zone B allows for significantly more stimulated volume in zone B than zone A (shallowest zone). A wide range of fracture orientations and high fracture density make zone C and zone D the most favorable zones for stimulation (intermediate zones). The BHTV did not reach the depth of zone E, however, zone E has a lower fracture density when compared to zones B, C and D. Thus, in this study we choose zone B as

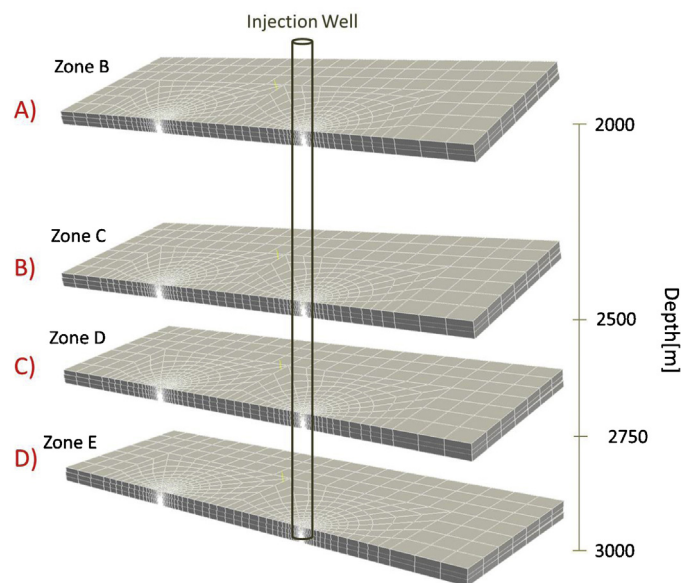


Fig. 2. Geometric layout of EGS reservoir for Newberry defined as four different zones (shallow to deep) and at four different depths of 2000, 2500, 2750 and 3000 m. (A) Reservoir is located at shallow zone B (2000 m depth). (B) Reservoir is located at intermediate zone C (2500 m depth). (C) Reservoir is located at intermediate zone D (2750 m depth). (D) Reservoir is located at deepest zone E (3000 m depth).

Table 2
Summary of zones based on parameters observed in NWG 55-29.

| Zone | Depth range (m) | Thickness (m) | Fracture count | Fracture density/meter | Lithology |
|------|-----------------|---------------|----------------|------------------------|--|
| A | 1966–2000 | 34 | 5 | 0.06 | Primary: welded lithic tuff Secondary: other tuff |
| B | 2000–2440 | 440 | 173 | 0.4 | Primary: tuffs Secondary: basalt, andesite |
| C | 2440–2633 | 193 | 157 | 0.8 | Primary: basalt, basaltic andesite |
| D | 2633–2908 | 275 | 16 | 0.06 | Primary: microcrystalline granodiorite Secondary: basalt, one large |
| E | 2908–3066 | 158 | No data | No data | Primary: basalt |

Table 4

Fracture data that utilized in the simulation.

| Fracture characterization | Unit | Depth (m) | | | |
|---------------------------------------|-----------------|-----------------------|---------------------|---------------------|----------------|
| | | 2000 Zone B | 2500 Zone C | 2750 Zone D | 3000 Zone E |
| Density of small fractures | m^{-1} | 0.5 | 0.9 | 0.9 | 0.26 |
| Density of large fractures | m^{-1} | 0.003 | 0.003 | 0.003 | 0.003 |
| Number of seeded fractures | – | 1000 | 1800 | 1800 | 600 |
| Initial permeability | m^2 | 1.6×10^{-17} | 3×10^{-17} | 3×10^{-17} | 10^{-17} |
| Fracture size | m | 10–1200 | 10–1200 | 10–1200 | 10–1200 |
| Fracture azimuth | ° | 0–360 | 0–360 | 0–360 | 0–360 |
| Fracture spacing | m | 1–300 | 1–300 | 1–300 | 1–300 |
| Standard deviation ($\bar{\sigma}$) | – | 19 | 19 | 19 | 19 |
| Mean ($\bar{\mu}$) | – | 360 | 360 | 360 | 360 |

the shallowest zone, zones C and D as an intermediate zone and zone E as the deepest zone. Boundary stresses that are utilized in the simulation for these four depths are defined in Table 3. The other difference between these zones is related to the fracture density and orientation. In the following section we explain how the fracture spacing, density and orientation for the shallow to deep reservoir are defined (Fig. 2).

2.2. Fracture networks model

Our numerical experiments are conducted for different zones (B, C, D and E). We use BHTV data to determine the frequency and orientation of natural fractures that are representative of the reservoir. These are then used to build the fracture network models used in the analysis. Fracture permeability changes can be approximated by change in the hydraulic aperture. The hydraulic aperture is calculated from the fracture spacing and initial permeability by a cubic law relation. The flow regime is evaluated from:

$$Q = \frac{A}{\mu} k \frac{dp}{dx} = \frac{dp}{dx} \frac{A}{\mu} \left(\frac{b_0^3}{12s_1} + \frac{b_0^3}{12s_2} + \dots + \frac{b_0^3}{12s_n} \right) \frac{dp}{dx}$$

where Q is fluid flow, k is permeability, A is cross-sectional area to flow and the dp/dx is pressure drop along fractures and μ is viscosity. b_0 is a initial hydraulic aperture and b_0 is calculated from: $b_0 = \sqrt[3]{12k_0s}$, where k_0 is initial permeability and s is spacing between fractures.

This shows when the fracture spacing is larger the hydraulic aperture is larger. Shear dilation during hydraulic and thermal process changes the hydraulic aperture and ultimately enhances the permeability.

The reservoir is assumed filled with various fracture sizes: Fracture lengths are in the range 10–1200 m and are also distributed with a Gaussian distribution (Bryc, 1995). This is defined as

$$f(\bar{x}, \bar{\mu}, \bar{\sigma}) = \frac{1}{\bar{\sigma}\sqrt{2\pi}} e^{-(1/2)(\bar{x}-\bar{\mu})/\bar{\sigma}^2} \quad (1)$$

where e is Euler's number, \bar{x} is a normal random variable, $\bar{\sigma}$ is the standard deviation and $\bar{\mu}$ is the mean. Small fractures (10–200 m) are distributed randomly within the volume both vertically and

horizontally and with multiple azimuthal orientations (π to 2π). Large fractures (200–1200 m) are rotated relative to the orientations of the principal stresses. For all fractures, failure is calculated from the evolution of shear and normal stresses recovered from the finite difference model FLAC^{3D}.

We distinguish a set of long and widely spaced fractures with infilling from a set of short and closely spaced fractures. Our best estimate for the network is given in Fig. 3. The shallow (B), intermediate (C and D) and deepest (E) zones have different densities of the closely spaced fractures (more closely spaced in the deeper zones C and D) but the same network of large fractures (density of 0.003 m^{-1} and spacing 300 m) (Fig. 3) is present. The more closely spaced fractures have densities of 0.5 m^{-1} in the shallow zone B, 0.9 m^{-1} in the intermediate zones C and D and 0.26 m^{-1} in the deepest zone E (Fig. 3). The fracture structure is defined based on orientation, size and number of fractures to determine the induced seismicity during stimulation.

3. Stress drop distribution during reservoir stimulation

We represent a model for evolution of strength and brittle failure on a pre-existing fracture as a stress drop. Shear failure calculations are handled with FLAC^{3D} utilizing a Mohr-Coulomb failure (fracture propagation is not considered). The friction angle on fractures is assumed constant (35°) and during failure the maximum shear stress drop ($\sim 3.0 \text{ MPa}$) is prescribed to represent the residual strength.

Stress drops resulting from the anticipated fracture networks are shown in Fig. 4 (mean spacing 300 m). Fig. 4B and C shows the denser networks (zones C and D), Fig. 4A illustrates the shallowest zone (B) and Fig. 4D illustrates the deepest zone (E) with the lowest fracture density. In all simulations we considered a single injector and observe that the stress drop along the large fractures is capped at the prescribed stress drop, τ . However for all the models with various fracture densities the mean stress drop is limited to be smaller than the maximum prescribed stress drop.

We observe during the short term stimulation that the development of stress drop begins earlier, reaches further from injection in a given time (~ 21 days) and is completed fastest for zones C and D with the largest fracture density (0.9 m^{-1}). This results because the more closely spaced fractures allow the more rapid removal of heat from the matrix blocks and the thermal migration occurs more rapidly and progresses more quickly. This allows failure to occur with smaller stress drops, rather than for the sharper thermal front migrating in the system with larger fracture spacing.

This larger reactivated domain within the reservoir may trigger seismicity and enhance the permeability during stimulation. We conclude that a significant factor in predicting the evolution of seismic events and permeability with time and location is related to the location, time and magnitude of such a stress drop.

Table 5

Initial volume fraction of reactive minerals in host reservoir.

| Mineral | Volume fraction of solid rock | |
|------------------|-------------------------------|----------------|
| | Granodiorite | Fractured vein |
| Anorthite | 0.33 | – |
| Calcite | 0.02 | 0.31 |
| Chlorite | – | 0.23 |
| K-feldspar | 0.17 | – |
| Quartz | 0.34 | 0.17 |
| Amorphous silica | – | – |

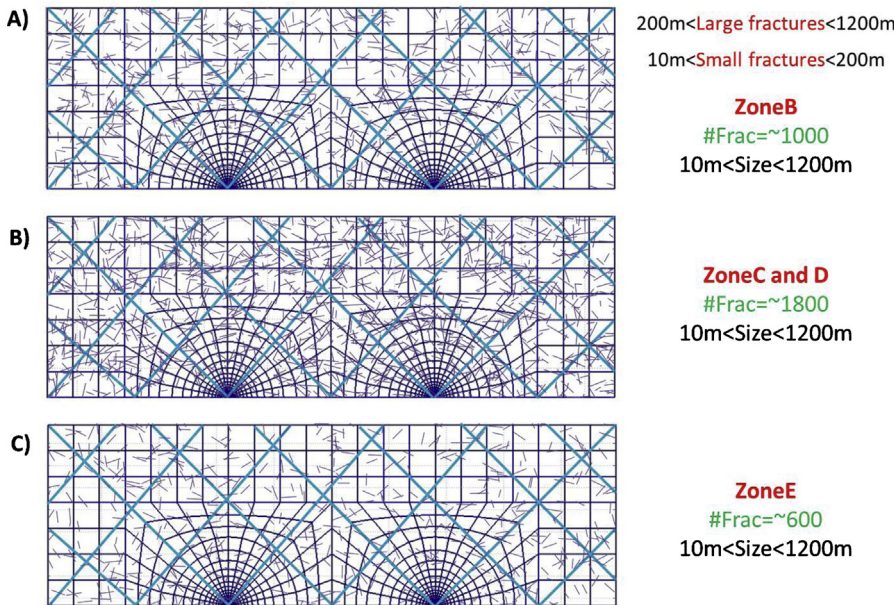


Fig. 3. Fracture network structure for the Newberry EGS reservoir, fracture size varies between 10 m and 1200 m. The same network of large fractures (density of 0.003 m^{-1} and spacing 300 m) defined for zone B, C, D and E. (A) The more closely spaced fractures have densities of 0.5 m^{-1} in the shallow zone B. (B) Fracture density of 0.9 m^{-1} applied in the intermediate zones C and D. (C) Fracture density of 0.26 m^{-1} applied in the deepest zone E.

4. Permeability evolution during short term stimulation

It is of interest to evaluate the evolution of hydraulic, thermal and mechanical effects and to deconvolve the dominant mechanisms with time and location. The THMC model is capable of linking the alteration of fluid transport and thermal transfer subject to the injection of a cold fluid. The hydraulic pressurization may have a near immediate effect and thermal transfer rate is then much slower than the hydraulic effect. Permeability evolution is related to the change of such hydraulic, thermal and mechanical effects in EGS reservoirs.

Fig. 5 is a comparison of how average radial matrix permeability changes at different depths (shallow to deep) and for different fracture structures (low to high density) by the end of stimulation. The contours of permeability (**Fig. 5A and C**) at each depth define the spatial distribution of reservoir permeability enhancement due to the contribution of the thermo-hydraulic mechanism. The permeability enhancement is concentrated along the direction of the large fractures that intersect the well and grows with time. Mechanical shearing on these major fractures (dilation angle is 10°) occurs due to the change in effective stress driven by fluid and thermal effects and their influence on reservoir shear failure. Since the fluid pressure distribution is anticipated to reach a steady state rapidly upon application, the migration with time represents a significant thermoelastic effect.

It is clear that for the widely spaced fracture network (shallow zone B and deepest zone E) (**Fig. 5A and D**), the increase in permeability reaches a smaller radius from the injection point and permeability evolution is slower with time compared to the behavior of the closely spaced fracture network (**Fig. 5B and C**). **Fig. 5E** shows reservoir permeability change at a cross section from the injection well after 21 days of stimulation in the shallow and deep zones. **Fig. 5E** shows clearly how this penetration corresponds to the population of small fractures around the injection well with permeability increased by one order of magnitude even after this short-term stimulation.

This behavior occurs because for the closely spaced fractures (zones C and D), transport of fluid pressure and thermal drawdown

in individual blocks is much faster than for the network of widely spaced fractures (zones B and E). As a result the fluid propagates faster with distance for the closely spaced fractures as observed for zones C and D in a given time. Thus the permeability enhancement for the closely spaced network (zones C and D) is both larger and reaches further from the injection well when compared to the wider-spaced network (zones B and E). Permeability improvement in all zones is not radially symmetric as it is related to the shear-induced permeability along the population of large fractures that intersect the injection borehole.

We show the evolution of reservoir permeability with time for the widely spaced (zone B) and closely spaced fracture (zone D) networks in **Fig. 6**, to compare the rate of permeability enhancement for shallow and deep zones with low (0.5 m^{-1}) and high (0.9 m^{-1}) fracture densities. **Fig. 6A** shows the response of the shallow reservoir (zone B) with a fracture density of 0.5 m^{-1} and compares this with the response of the deeper reservoir (zone D) with a higher fracture density (0.9 m^{-1}) (**Fig. 6C**). We observe that by increasing the fracture density from 0.5 to 0.9 m^{-1} , the evolution of permeability occurs approximately twice as rapidly as for the 0.5 m^{-1} density fracture network (**Fig. 6C**) and reaches further into the reservoir at any given time. **Fig. 6B and D** shows how this barrier corresponds to the fracture spacing around the injection well. We observe that the widely spaced fracture network at shallow zone B experiences less enhancement with radius at any given time (21 days stimulation) compared to the closely spaced fracture network in the deeper zone D. This relates to the faster thermal drawdown reaching to a larger radial distance from the injection point due to development of a larger connective path at intermediate depth (zones C and D).

Such changes in permeability may stimulate the fracture networks especially near the injection point and produce large and early seismic events. The following section explains the relation between permeability evolution and induced seismicity to examine how permeability enhancement during short-term stimulation influences the magnitude of seismic events for different characteristics of the fracture networks and stress regimes at different locations within the reservoir.

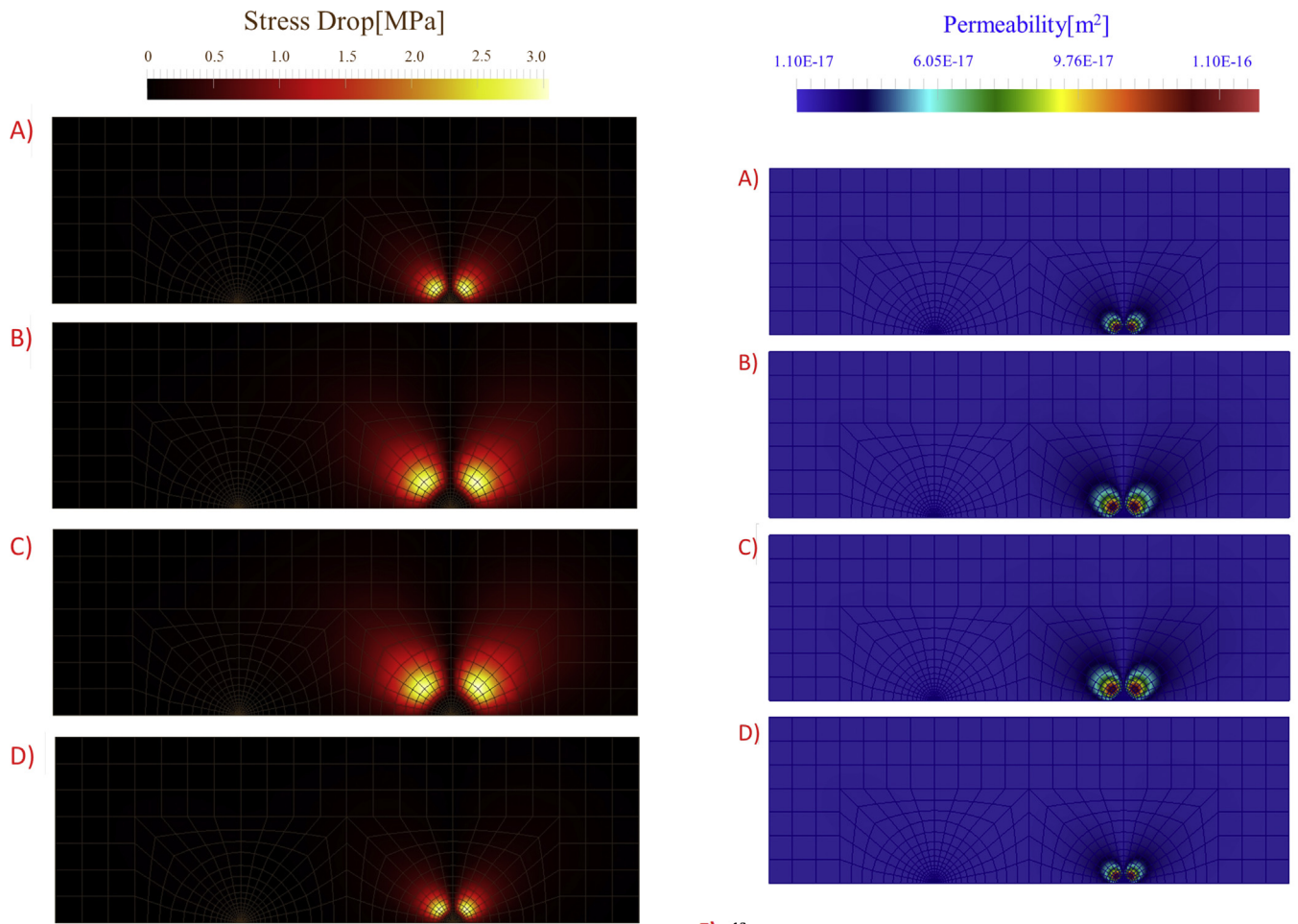


Fig. 4. Development of stress drop at four different zones (shallow to deep) and at four different depths of 2000, 2500, 2750 and 3000 m after 21 day stimulation. The same network of large fractures (density of 0.003 m^{-1} and spacing 300 m) applied in each zone. (A) The more closely spaced fractures have densities of 0.5 m^{-1} in the shallow zone B. (B) Intermediate zone C with 0.9 m^{-1} fracture density. (C) Intermediate zone D with 0.9 m^{-1} fracture density. (D) Deepest zone E with 0.26 m^{-1} fracture density.

5. Evolution of moment magnitude during stimulation

The potential energy released within reservoirs for closely and widely spaced fracture networks is defined based on the evaluation of the elastic energy released from repeating failures of large penny-shaped fractures. The potential release of energy for different fracture networks is calculated by the summation of elastic energy released on individual penny-shaped fractures absent mechanical interaction. The potential energy release, E_p , is defined as

$$E_p = \frac{2\Delta\tau^2 a^3}{3G} \quad (2)$$

where $\Delta\tau$ is the shear stress drop, a is the radius of the fracture in the plane of the fracture and G is shear modulus. Energy release from a pre-existing fracture increases with the square of the stress drop and the cube of the fracture size. This energy release is triggered by the evolving stress state due to pore pressures and induced thermal and chemical strains.

Energy release from fractures is most conveniently represented as a moment magnitude (Aki, 1967; Kanamori, 1977; Keyliss-Borok,

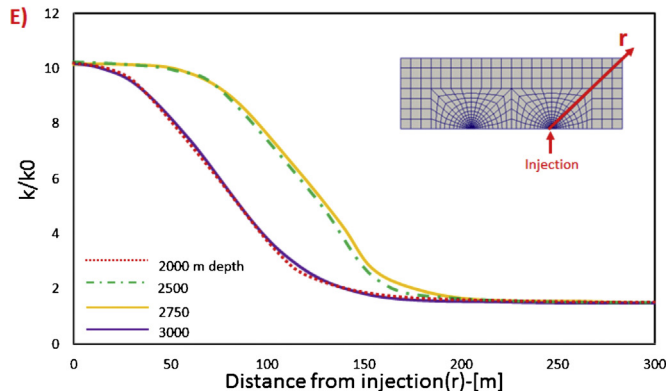


Fig. 5. Evolution of permeability in four different zones (shallow to deep) and at four different depths of 2000, 2500, 2750 and 3000 m after 21 day stimulation. The same network of large fractures (density of 0.003 m^{-1} and spacing 300 m) applied at each zone. (A) The more closely spaced fractures have densities of 0.5 m^{-1} in the shallow zone B. (B) Intermediate zone C with 0.9 m^{-1} fracture density. (C) Intermediate zone D with 0.9 m^{-1} fracture density. (D) Deepest zone E with 0.26 m^{-1} fracture density. (E) Permeability change along the radius (r) where long fracture is located in the shallow and deep zones.

1959). The moment magnitude relation is defined as (Purcaru and Berckemer, 1978):

$$\log M_0 = 1.5M_s + 9.1 \quad (3)$$

where M_0 is seismic moment and M_s is moment magnitude. In this model M_0 is the seismic energy that is derived from the elastic energy released by shear on pre-existing fractures.

We determine the spatial/temporal evolution of moment magnitude in the reservoir for the ensemble arrangement of fractures

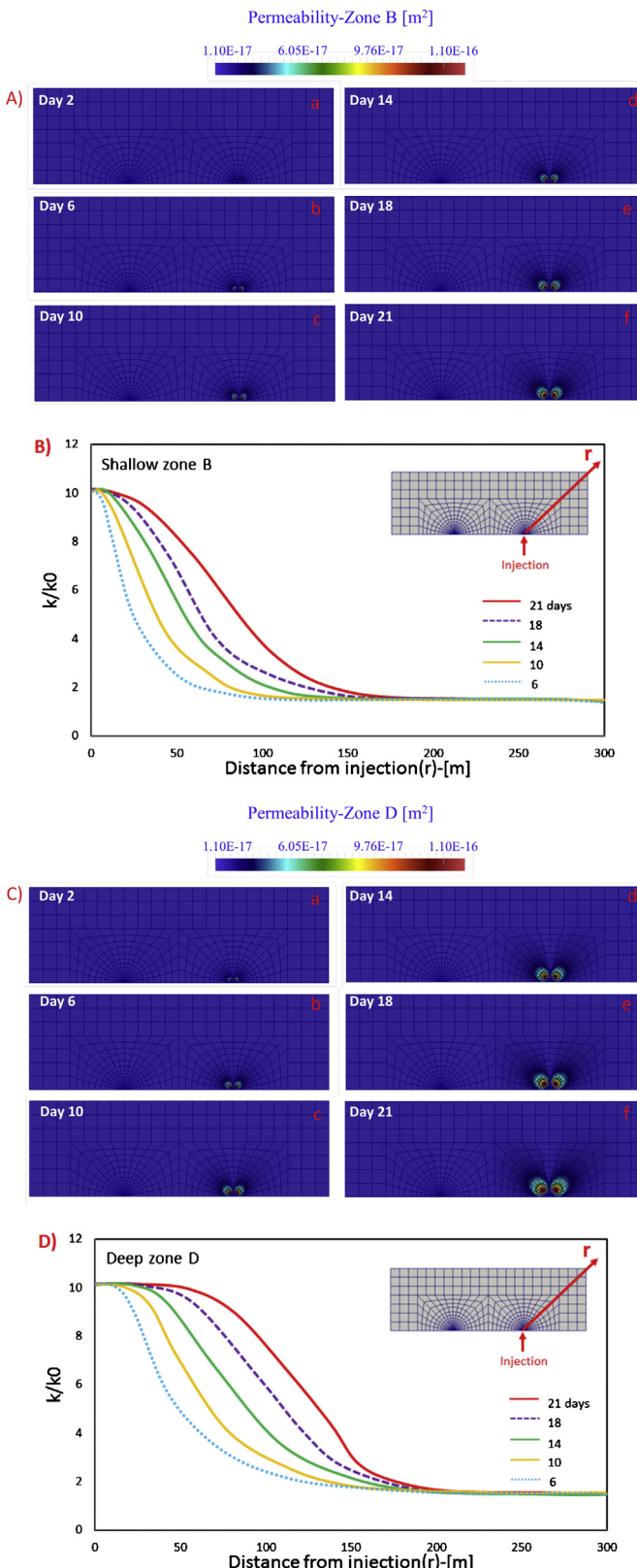


Fig. 6. Evolution of permeability during short stimulation (21 days) for shallow zone B at 2000 m depth and intermediate zone D at 2750 m depth. Windows a, b, c, d, e and f show the permeability enhancement with time. The same network of large fractures (density of 0.003 m^{-1} and spacing 300 m) applied at both zones. (A) The more closely spaced fractures have densities of 0.5 m^{-1} in the shallow zone B. (B) Permeability change along the radius (r) where long fracture is located after 21 days stimulation at shallow zone B. (C) Intermediate zone D with 0.9 m^{-1} fracture density. (D) Permeability change along the radius (r) where large fracture is located at

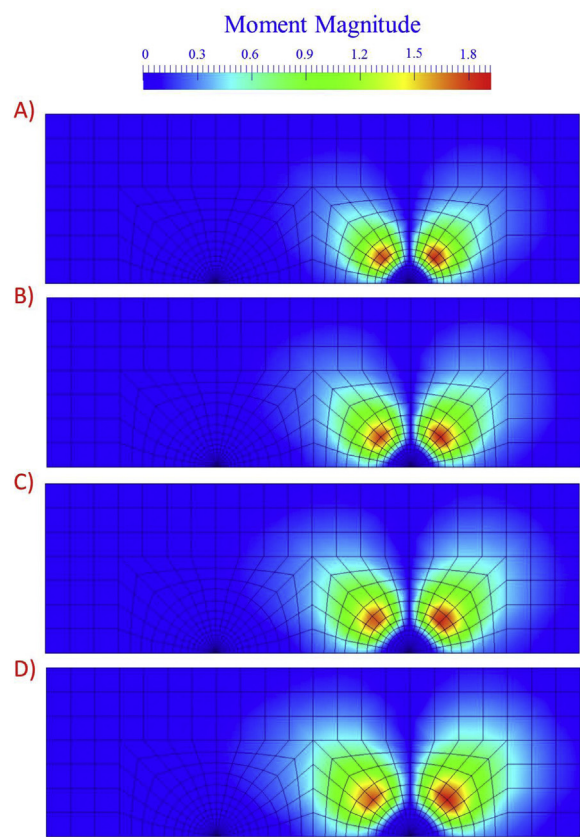


Fig. 7. Evolution of moment magnitude at four different zones (shallow to deep) and at four different depths of 2000, 2500, 2750 and 3000 m after 21 day stimulation. The same network of large fractures (density of 0.003 m^{-1} and spacing 300 m) and also the same network of closely spaced fractures (densities of 0.9 m^{-1}) applied at each zone. (A) Reservoir at shallow zone B. (B) Intermediate zone C. (C) Intermediate zone D. (D) Deepest zone E.

by using the above relations in Fig. 7. For minimum (10 m) and maximum (1200 m) fracture radii, a maximum shear stress drop of $\sim 3 \text{ MPa}$ and a shear modulus of 10 GPa, the evaluated magnitude of events, M_s varies from -2 to $+1.9$. The largest event size (~ 1.9) corresponds to the largest fracture size ($\sim 1200 \text{ m}$) within the reservoir.

During the evolution of energy release the principal difference between zones is related to the fracture density as well as the incremental stress drop that is realized and accompanies failure. The largest stress drop occurs along the large fractures and this extends furthest in comparison to that for the smaller fractures.

We observe that the contours in Fig. 7 are not radially distributed due to the presence of the large pervasive fractures. When we compare the potential energy released in the different zones (shallow to deep), we observe that this release begins and builds earlier, reaches further from the injection in a given time and is completed faster for intermediate zones (C and D) with the largest fracture density (0.9 m^{-1}) compared to the zones with the smaller fracture density (B (0.5 m^{-1}) and E (0.26 m^{-1})).

We then use a stress-strain fracture criterion to determine the total strain energy available for release – this energy is assumed to be shed seismically. During the rupture process the shear stress

deep zone D. (A and B) Shallow zone B and fracture geometry of Fig. 3A, a, b, c, d, e, f shows the permeability enhancement with time. (C and D) Deep zone D and fracture geometry of Fig. 3B, a, b, c, d, e, f shows the permeability enhancement with time.

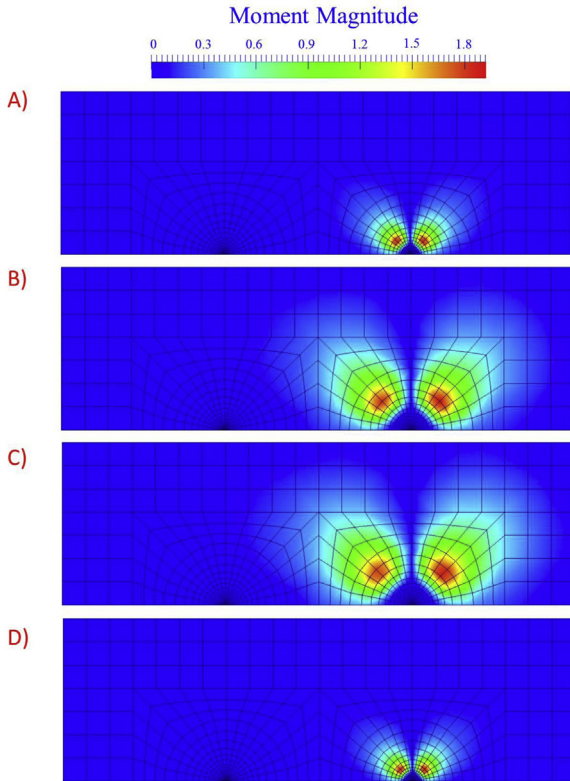


Fig. 8. Evolution of moment magnitude at four different zones (shallow to deep) and at four different depths of 2000, 2500, 2750 and 3000 m after 21 day stimulation. The same network of large fractures (density of 0.003 m^{-1} and spacing 300 m) applied at each zone. (A) The more closely spaced fractures have densities of 0.5 m^{-1} in the shallow zone B. (B) Intermediate zone C with 0.9 m^{-1} fracture density. (C) Intermediate zone D with 0.9 m^{-1} fracture density. (D) Deepest zone E with 0.26 m^{-1} fracture density.

drops an amount $\Delta\tau$ from an initial value of τ_i to a final value τ_f . The total energy is

$$E_T = \int \Delta\tau^T \Delta\varepsilon dV$$

where strain changes from an initial value of ε_i to a final value ε_f where V is volume of the matrix. Here we introduce a relation to determine the number of events which occur during the failure process based on potential and total energy as

$$N_{\text{event}} = \frac{E_T}{E_p}$$

where N_{event} is the number of seismic events, E_T is the total energy and E_p is the potential energy. Simulation results are presented in a manner analogous to the conceptual models of various fracture networks (Fig. 3) at shallow depth and intermediate fracturing (zone B with 0.5 m^{-1} density), intermediate depth and the greatest fracturing (zones C and D with 0.9 m^{-1} density) and the deepest zone that is least fractured (E with 0.26 m^{-1} density).

The outcomes for induced seismicity and permeability evolution for these different cases allow comparison of the effects of various fracture spacings and stress states as a result of reservoir stimulation. For more closely spaced fractures, the migration rate of seismic events is faster, the event rate is higher and the integrated energy release is also larger than for more widely spaced fractures. That this larger cumulative energy is released in a larger number of small events is useful in limiting both event size and the related apparent influence of felt seismicity.

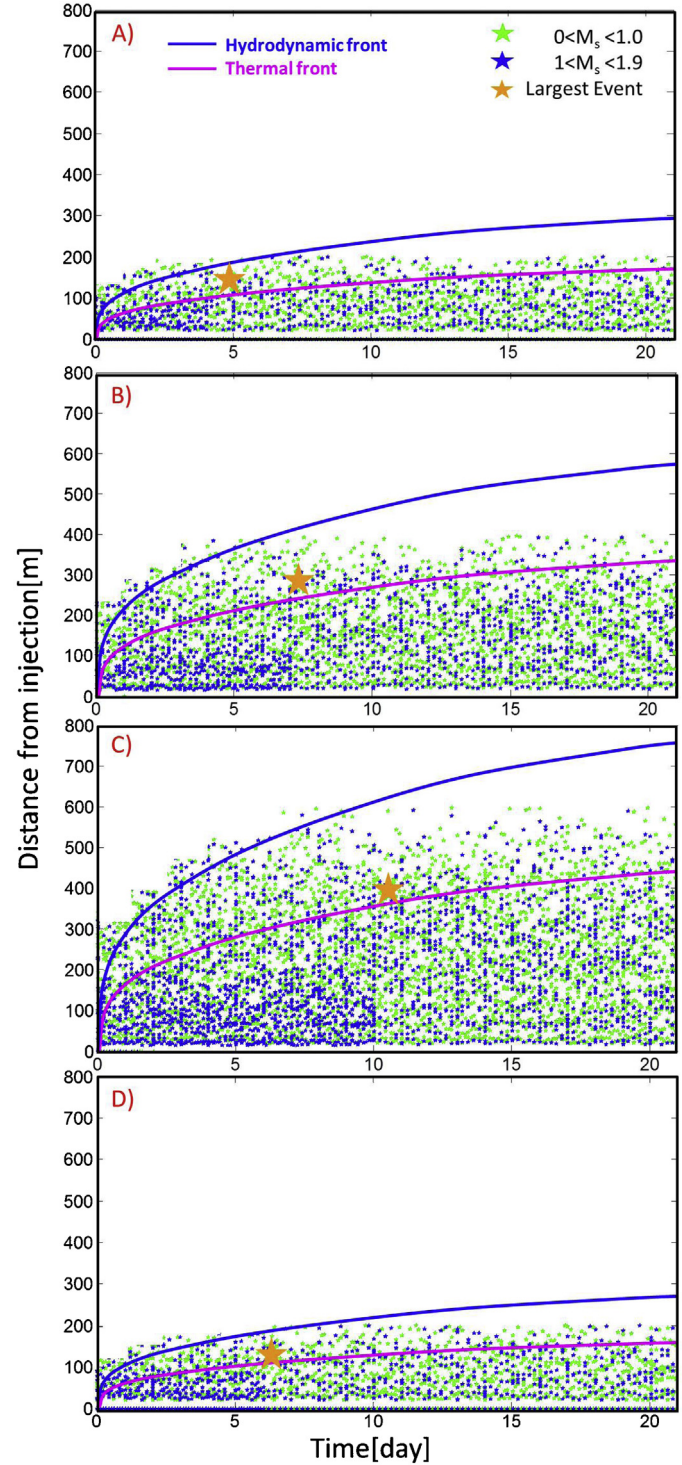


Fig. 9. Radius versus time plot for short term of the progress of fluid and thermal fronts in the reservoir and of induced seismicity (injection flow rate is 44 l/s). Seismic moment of individual events shown green: $0 < M_s < 1$ and blue: $1 < M_s < 1.9$ and the largest event is ~ 1.9 shown with orange star. Reservoir located at four different zones (shallow to deep) and at four different depths of 2000, 2500, 2750 and 3000 m after 21 day stimulation. The same network of large fractures (density of 0.003 m^{-1} and spacing 300 m) applied at each zone. (A) The more closely spaced fractures have densities of 0.5 m^{-1} in the shallow zone B. (B) Intermediate zone C with 0.9 m^{-1} fracture density. (C) Intermediate zone D with 0.9 m^{-1} fracture density. (D) Deepest zone E with 0.26 m^{-1} fracture density. (For interpretation of the references to color in this figure legend, the reader is referred to the web version of the article.)

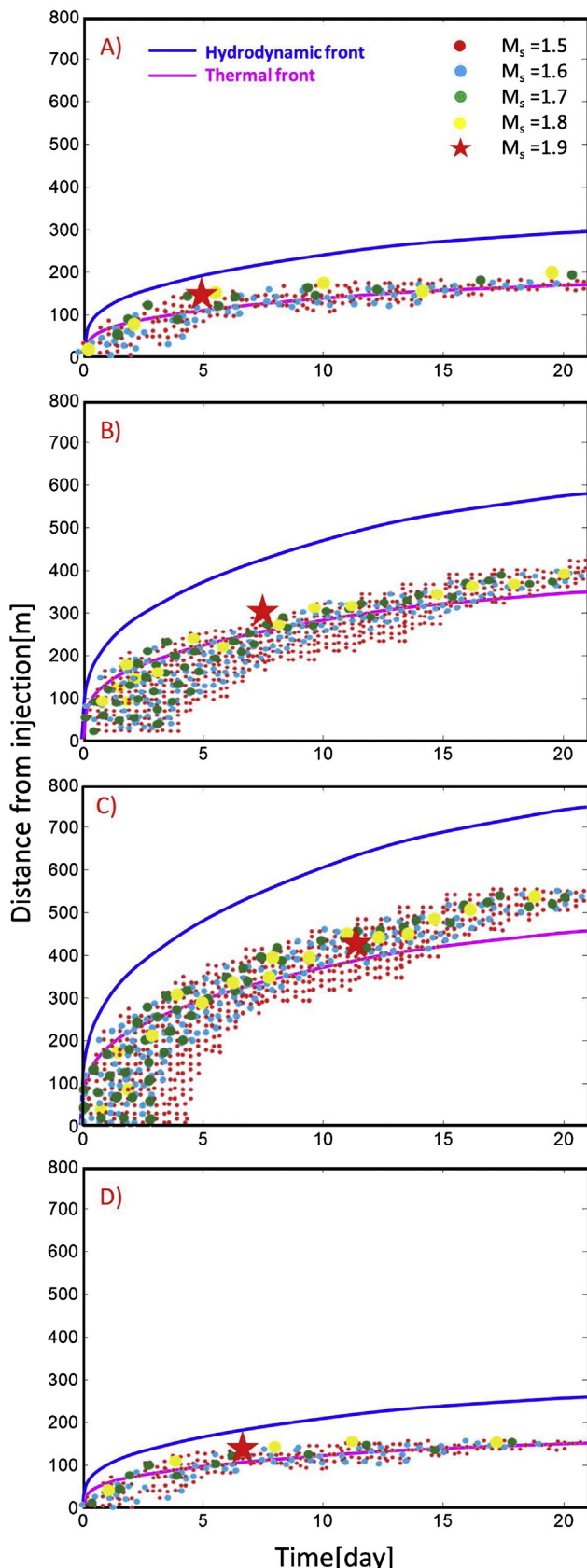


Fig. 10. Radius versus time plot for short term of the progress of fluid and thermal fronts in the reservoir and of induced seismicity (injection flow rate is 44 l/s). Reservoir located at four different zones (shallow to deep) and at four different depths of 2000, 2500, 2750 and 3000 m after 21 day stimulation. The same network of large fractures (density of 0.003 m^{-1} and spacing 300 m) applied at each zone. Larger seismic moment of individual events shown red: $M_s = 1.5$, blue: $M_s = 1.6$, green: $M_s = 1.7$,

yellow: $M_s = 1.8$ and the largest event is ~ 1.9 shown with red star. (A) The more closely spaced fractures have densities of 0.5 m^{-1} in the shallow zone B. (B) Intermediate zone C with 0.9 m^{-1} fracture density. (C) Intermediate zone D with 0.9 m^{-1} fracture density. (D) Deepest zone E with 0.26 m^{-1} fracture density. (For interpretation of the references to color in this figure legend, the reader is referred to the web version of the article.)

The characteristic event magnitude distribution that occurs in these cases is defined based on the size and location of fractures. The largest events occur close to existing large and widely spaced fractures where stress drop reaches the maximum magnitude $\sim 3 \text{ MPa}$. Thus the energy release from these large ($\sim 200\text{--}1200 \text{ m}$) but widely spaced fractures within the reservoir determines the evolution of the principal seismic event magnitude and ultimately can give significant information about the rate of propagation with time.

To determine the sensitivity of the evolution of seismic event size, rate, and position to the evolution of effective stress relative to initial stress state we examine the behavior first for the same fracture network (with 0.9 m^{-1} density) and the stresses of zones B (2000 m), C (2500 m), D (2750 m) and E (3000 m). We then explore behavior for the stresses of zones B (2000 m), C (2500 m), D (2750 m) and E (3000 m) but for the different fracture densities of zones B (0.5 m^{-1}), C (0.9 m^{-1}), D (0.9 m^{-1}) and E (0.26 m^{-1}).

5.1. Influence of effective stress evolution of moment magnitude

The performance of our model – specifically following the progress of seismicity within the reservoir – is developed in terms of rates, magnitudes and locations of events and examined against observational data for two geothermal fields: Cooper Basin (Australia) and Coso geothermal field (USA) (Izadi and Elsworth, 2013). We observed good agreement between our model observations and those in the Cooper Basin (Shapiro and Dinske, 2009a,b).

We now consider the key influence of stress state on induced seismicity when the same fracture network (high density – 0.9 m^{-1}) applies within the reservoirs but at shallow depths (2000 m zone B) to greater depths (3000 m zone E). This examines the stress-sensitivity of the reservoir during reservoir stimulation (~ 21 days). The denser fracture network (closely spaced fracture) of zones C and D provides the probability of largest seismic events during stimulation – thus we select this highest fracture density network (0.9 m^{-1}) in this study. A representation of the fracture network geometry is shown in Fig. 3B. In all simulations, the only parameter that varies is the stress magnitude according to the regime ($S_{\text{hmin}} = 0.75 S_{\text{v}}$).

The seismic energy released during the stimulation is illustrated in Fig. 7. We observe a large migration of energy release as a significant population of seismic activity exists near injection and along the large fractures. Such seismic events migrate more rapidly at any given time outward from the injection point and reaching to a larger distance when the stresses on the stimulation target is largest, corresponding to the deepest zone (zone E at 3000 m). But this analysis shows that by increasing the stress (reaching the deeper reservoir) the migration rate of seismic events with time and location changes little. Thus, these events may form at the same rate for shallow to deep zones when the same fracture network is applied.

5.2. Influence of fracture structure on evolution of moment magnitude

We contrast the response for an invariant fracture network but with changing stress level (previous) with that for a constant initial stress but for different realizations of fracture network densities. This analysis is based on low (zone E $\sim 0.26 \text{ m}^{-1}$), intermediate (zone B $\sim 0.5 \text{ m}^{-1}$), and high (zones C and D $\sim 0.9 \text{ m}^{-1}$) fracture densities representing ranges of total numbers of 600–1800

yellow: $M_s = 1.8$ and the largest event is ~ 1.9 shown with red star. (A) The more closely spaced fractures have densities of 0.5 m^{-1} in the shallow zone B. (B) Intermediate zone C with 0.9 m^{-1} fracture density. (C) Intermediate zone D with 0.9 m^{-1} fracture density. (D) Deepest zone E with 0.26 m^{-1} fracture density. (For interpretation of the references to color in this figure legend, the reader is referred to the web version of the article.)

fractures filling the half-reservoir. The fracture schemes that are used in simulations are displayed in Fig. 3. For all zones we calculate the potential energy release of fractures to determine the moment magnitude evolution during short-term stimulation (Fig. 8).

We observe that the rate of seismic event migration within the reservoir is controlled principally by the density and spacing of the fractures. For various fracture network models (low to high density) the seismic event rate increases with increased fracture density (i.e. zones C and D with 0.9 m^{-1}) and is largely independent of stress level.

The model with the highest fracture density Fig. 8B and C generates both the most and the largest seismic events ($M_s = 1.9$) within the 21 day stimulation time window. Absolute stress is largest when the stimulation target is deeper but stress drop is limited by the difference in peak and residual strength of the fractures ($\sim 3 \text{ MPa}$) and hence cannot be a critical parameter (Fig. 8D). The reason for this behavior is related to the cumulative energy release of the fractures which scales with the size of fractures comprising the network and a roughly constant magnitude of stress drop.

We note that the rate of hydraulic and thermal transport has a considerable influence on the severity, location and timing of failure in all our models. The event rate is highest when the fracture network has the largest density (0.9 m^{-1}) and is located at depth where the initial stresses are highest (zone D). In the next section we separately explore the influence of events driven by fluid pressure or due to thermal destressing in fractured reservoirs.

6. Hydrodynamic and thermal front triggering of seismicity

We attempt to understand the mechanisms of seismic triggering due to fluid and thermal effects by correlating the evolution of seismicity with the transit of the hydrodynamic and thermal fronts during the 21 day stimulation. We follow the propagation of the fluid pressure, thermal and chemical fronts through the reservoir with time and determine associations of events with the various causal mechanisms.

The numerical model is used to follow the hydrodynamic and thermal fronts as they propagate through the reservoir for various fracture networks (low to high density) at low and high (shallow to deep zones) initial stresses. The location of these fronts is defined by the propagation of the fluid flow rate at any given time. The evolution of seismicity for the short-term stimulation is shown in a radius-time plot relative to the propagation of these fluid and thermal fronts in Fig. 9 (injection flow rate is set at $441/\text{s}$ in the simulation). This shows the progress of the fluid and thermal fronts in the reservoir together with the progress of induced seismicity. We observe that the rate of propagation of the hydrodynamic front is approximately twice as rapid as the thermal front.

The deepest penetration of the hydrodynamic front into the reservoir at any given time is recorded for the network with the most closely spaced fractures at the intermediate depths of zones C (2750 m) and zone D (3000 m) (Fig. 9B and C). This increased penetration could result from two mechanisms. (i) The first is due to the immediate increase in fluid pressure and drop in effective stresses that allows the fractures to dilate. Where the initial permeabilities of the closely and widely spaced fracture networks are initially the same, a unit change in effective stress will result in a larger permeability change for the more closely spaced network. This is because the ratio of change in aperture to initial aperture ($\Delta b/b_0$) is larger for the more closely spaced network since aperture change is the same in each case (for constant fracture stiffness). (ii) In addition, if temperatures are able to change significantly during the stimulation period, this response will be fastest for the most closely spaced fractures due to the (thermally) diffusive length scale defined by fracture spacing (Elsworth, 1989b; Elsworth and Xiang, 1989). As

we illustrate in Fig. 9 the largest event occurs at different times at each zones. The largest event occurs at the location (outward from injection) where the stress drop is highest and on the largest fracture.

To further understand the evolution of induced seismicity in space and time we separately indicate the larger event magnitudes ($M_s \sim 1.5\text{--}1.9$) in Fig. 10. Fig. 10A–D illustrates the progress of the fluid and thermal fronts in zones B, C, D and E (shallow to deep). Events are separated into four magnitude classifications and the largest event magnitude is also shown. We observe that the number of seismic events decays with time and distance from the injection point at each reservoir. This illustrates that most of the seismic activity is triggered by hydraulic effects at early times relative to

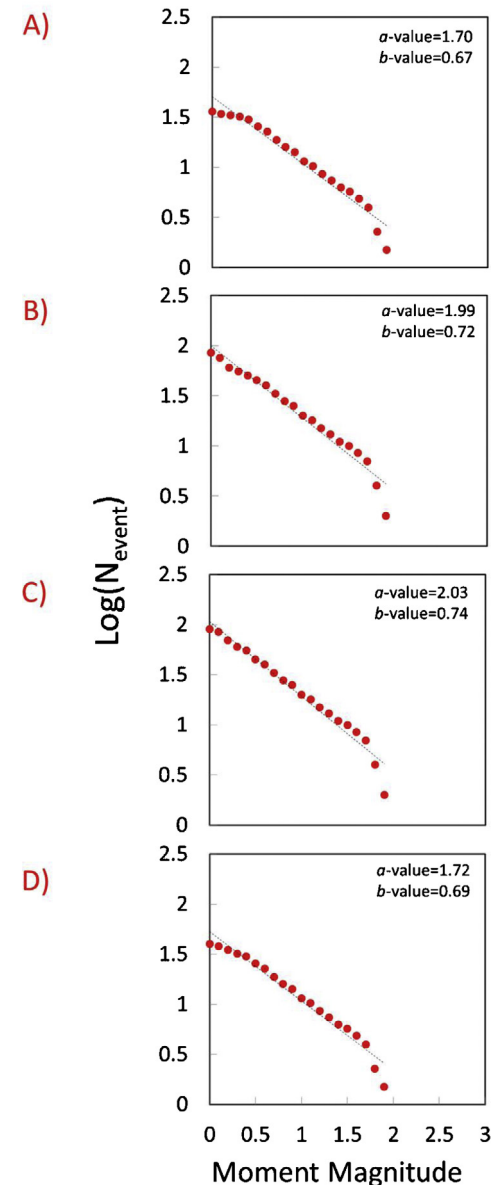


Fig. 11. Number of events as a function of magnitude indicating b -value for moment magnitudes in the range 0–1.9 after 21 days stimulation. Reservoir located at four different zones (shallow to deep) and at four different depths of 2000, 2500, 2750 and 3000 m. The same network of large fractures (density of 0.003 m^{-1} and spacing 300 m) applied at each zone. b -Values are evaluated for (A) the more closely spaced fractures have densities of 0.5 m^{-1} in the shallow zone B ($b \sim 0.67$). (B) Intermediate zone C with 0.9 m^{-1} fracture density ($b \sim 0.72$). (C) Intermediate zone D with 0.9 m^{-1} fracture density ($b \sim 0.74$). (D) Deepest zone E with 0.26 m^{-1} fracture density ($b \sim 0.69$).

the initiation of stimulation. At later time, thermal effects (and possibly chemical effects as well) may contribute to the seismicity when the seismicity front then lags behind the hydrodynamic front.

7. Empirical relation for seismicity occurrence

From the Gutenberg–Richter law we model the frequency–magnitude distribution. The modeled b -value represents the cumulative number of seismic events at each location within the reservoir with the local magnitude evaluated from its seismic moment. Gutenberg and Richter (1944) expressed the magnitude distribution in the form $\log N_{\text{event}} = a - bM$, where N_{event} is the number of seismic events within a magnitude interval $M \pm \Delta M$.

Here we discuss the scaling of the frequency of events N_{event} as a function of fluid pressure and temperature for stimulation at the Newberry EGS. The number of events as a function of time is controlled only by the cumulative mass of fluid injected which can cause failure and result in energy release. The greater this energy release the larger the number of events induced at a given location and therefore the greater the probability of large-magnitude events. Thus, the model above is able to predict magnitude–frequency distributions. We characterize the induced seismicity by the b -value for three different fracture geometries (high to low density) in Fig. 3A–C.

The anticipated approximate b -value for the Newberry EGS is illustrated in Fig. 11. Apparent from these data is that the closely spaced fracture network with the higher stress regime (at the deeper level) has the largest b -value ~ 0.74 (Fig. 11C). This shows the greater number of events induced due to the existence of a high density fracture network (0.9 m^{-1}) and under the prescribed conditions of higher in situ stresses. We observe the lowest b -value ~ 0.67 when we stimulate the shallow zone B with the intermediate and lower fracture density (0.5 m^{-1}). We conclude that the b -value describes fracture processes in the seismic region and is principally related to the fracture network density.

8. Conclusion

From our modeling experiments, permeability enhancement and induced seismicity within EGS reservoirs are each shown to be influenced by different factors during stimulation. In this study a variety of models are developed to understand the role of thermal-, hydraulic-, mechanical- and chemical-effects on different fractured reservoirs. Various fracture networks (low to high density) are considered and reservoir stress conditions are changed due to the depth of the reservoir (shallow to deep). We apply our models to the prospective Newberry EGS demonstration project (USA) to determine the effect of these key factors on permeability evolution and induced seismicity during the short-term (~ 21 day) stimulation of the reservoir.

We see penny-shaped fractures throughout the reservoir to define fracture stiffness and shear displacement within the reservoir. Energy release from a pre-existing large single fracture increases with the square of the stress drop and the cube of the fracture size. This energy release is triggered by the evolving stress state due to pore pressures and induced thermal and chemical strains. Effective normal stresses and pore pressures are altered during injection. Then potential energy from various fracture sizes is calculated to predict seismic event magnitudes.

We observe that permeability increases by an order of magnitude during stimulation. For the closely spaced fracture network (with 0.9 m^{-1} density) the increase of fluid circulation is higher and therefore the permeability change is propagated further from injection and occurs in shorter time than for more widely spaced

fractures. Likewise for the reservoir with the highest density of fractures and high initial stresses due to greater depth – the evolution of seismicity is more rapid (higher event rate) and its distribution expands fastest with radius (zone D).

A maximum event magnitude for identical fracture distributions is $M_s \sim 1.9$ and maximum shear stress drop is prescribed as $\sim 3 \text{ MPa}$. We use fluid pressures and reservoir temperatures as proxies to track the hydrodynamic and thermal fronts and to define causality in the triggering of seismicity. Larger events form due to higher flow rate at early time and at later time the thermal effect also exerts an influence on the rate of events as well as event magnitude.

We separately examine the effects of thermal stresses, pore pressure and chemical effects on the evolution of seismicity in reservoirs. The most important mechanism which triggers slip and promotes seismic events and also may change the moment is the augmentation of fluid pressure at the beginning of stimulation. The influence of thermal stress may determine the rate and magnitude of seismic events when the fluid pressure is changing less rapidly (after ~ 5 days). Thermal effects may be the reason for the faster propagation of events clouds for the more closely spaced fracture networks. The largest event occurs when the mean stress drop reaches the maximum prescribed stress drop ($\sim 3 \text{ MPa}$). Such behavior illustrates the propagation of fluid pressure and thermal fronts through the reservoir with time and associate large early-time events with the fluid front and later lower seismic magnitude events with the transit of the thermal (–chemical) front.

The b -value is also evaluated for different fracture networks at different depths. The b -value describes the fracture process within reservoirs and is related to size, location, distribution and spacing of fractures. We observe the largest b -value for the zone at intermediate stress level and with the greatest fracture density (zone D $\sim 0.9 \text{ m}^{-1}$). This represents the largest number of seismic events triggered with largest distribution in size. We illustrate that the penetration of the hydrodynamic front is principally controlled by the density and spacing of fractures. When we increase the density of fractures (i.e. more closely spaced fracture) in the system we allow the fluid flow to penetrate more rapidly during injection (zone D), thus the fluid penetrates further from the injection well at any given time. The rate of fluid penetration during injection influences the permeability evolution as well as the rate and magnitude of induced seismicity.

Acknowledgements

This work is the result of partial support from the Department of Energy Office of Energy Efficiency and Renewable Energy and Geothermal Technology Program under contract EE-10EE0002761. This support is gratefully acknowledged.

References

- Aki, K., 1967. Scaling law of seismic spectra. *J. Geophys. Res.* **72**, 1217–1231.
- Baisch, S.R., Voeroes, E., Rothert, H., Stang, R.J., Schellschmidt, R., 2010. A numerical model for fluid injection induced seismicity at Soultz-sous-Forêts. *Int. J. Rock Mech. Min. Sci.* **47** (3), 405–413, <http://dx.doi.org/10.1016/j.ijrmms.2009.10.001>.
- Bruce, R.J., Foulger, G.R., Monastero, F.C., 2009. Seismic monitoring of EGS stimulation tests at the Coso geothermal field, California, using microearthquake locations and moment tensors. In: Thirty-Fourth Workshop on Geothermal Reservoir Engineering Stanford University, Stanford, CA, February 9–11, SGP-TR-187.
- Bryc, W., 1995. *The Normal Distribution: Characterizations with Applications*. Springer-Verlag, ISBN 0-387-97990-5.
- Cladouhos, T., Petty, S.C., Osborn, W., Hickman, S., Davatzes, N., 2011. The role of stress modelling in stimulation planning at the Newberry volcano EGS demonstration project. In: Thirty-Sixth Workshop on Geothermal Reservoir Engineering, Stanford, CA.

- Dinske, C., Shapiro, S., Häring, M., 2010. Interpretation of microseismicity induced by time-dependent injection pressure. SEG Expanded Abstr. 29, 2125, <http://dx.doi.org/10.1190/1.3513264>.
- Elsworth, D., 1989a. Thermal permeability enhancement of blocky rocks: one-dimensional flows. Int. J. Rock Mech. Min. Sci. Geomech. Abstr. 26 (July (3–4)), 329–339.
- Elsworth, D., 1989b. Theory of thermal recovery from a spherically stimulated HDR reservoir. J. Geophys. Res. 94 (B2), 1927–1934.
- Elsworth, D., Xiang, J., 1989. A reduced degree of freedom model for permeability enhancement in blocky rock. Geothermics 18 (5/6), 691–709.
- Elsworth, D., Yasuhara, H., 2010. Mechanical and transport constitutive models for fractures subject to dissolution and precipitation. Int. J. Numer. Meth. Geomech. 34, 533–549, <http://dx.doi.org/10.1002/nag.831>.
- Evans, K., Moriya, H., Niitsuma, H., Jones, R., Phillips, W., Genter, A., Sausse, J., Jung, R., Baria, R., 2005. Microseismicity and permeability enhancement of hydrogeologic structures during massive fluid injections into granite at 3 km depth at the Soultz HDR site. Geophys. J. Int. 160 (1), 388–412, <http://dx.doi.org/10.1111/j.1365-246X.2004.02474.x>.
- Goodman, 1976. Methods of Geological Engineering in Discontinuous Rocks. West Publishing, New York, 472 pp.
- Gutenberg, B., Richter, C.F., 1944. Frequency of earthquakes in California. Bulletin of the Seismological Society of America 34, 185–188.
- Izadi, G., Elsworth, D., 2013. The effects of thermal stress and fluid pressures on induced seismicity during stimulation to production within fractured reservoirs. Terra Nova 25, Pp. 774–380.
- Jaeger, J.C., Cook, W.G.W., Zimmerman, R.W., 2007. Fundamentals of Rock Mechanics, fourth ed. Blackwell Publishing, Malden, MA, 475 pp.
- Kanamori, H., 1977. The energy release in great earthquakes. Geophys. Res. 82, 2981–2987.
- Keylis-Borok, V.I., 1959. On estimation of the displacement in an earthquake source and of source dimensions. Ann. Geofisic. 12, 205–214.
- Kovac, K.M., Xu, T., Pruess, K., et al., 2006. Reactive chemical flow modeling applied to injection in the Coso EGS experiment. Proceedings: Thirty-First Workshop on Geothermal Reservoir Engineering. Stanford University, Stanford, CA.
- Murphy, H., 1982. Hot dry rock reservoir development and testing in the USA. In: Proc. 1st Japan-U.S. Seminar on Hydraulic Fracturing and Geothermal Energy. Martinus Nijhoff, The Hague, pp. 33–38.
- Nemat-Nasser, S., 1982. Thermally induced cracks and heat extraction from hot dry rocks. In: Proc. 1st Japan-U.S. Seminar on Hydraulic Fracturing and Geothermal Energy. Martinus Nijhoff, The Hague, pp. 11–31.
- Pine, R.J., Cundall, P.A., 1985. Applications of the fluid–rock interaction program (FRIP) to the modelling of hot dry rock geothermal energy systems. In: Proc. Int. Symp. on Fundamentals of Rock Joints. Centek, pp. 293–302.
- Purcaru, G., Berckemer, H., 1978. A magnitude scale for very large earthquakes. Tectonophysics 49, 189–198.
- Renshaw, C.E., 1995. On the relationship between mechanical and hydraulic apertures in rough-walled fractures. J. Geophys. Res. 100, 24629–24636.
- Rutqvist, J., Wu, Y.S., Tsang, C.F., Bodvarsson, G., 2002. A modeling approach for analysis of coupled multiphase fluid flow, heat transfer, and deformation in fractured porous rock. Int. J. Rock Mech. Min. Sci. 39, 429–442.
- Shapiro, S.A., Dinske, C., 2007. Violation of the Kaiser effect by hydraulic-fracturing-related microseismicity. J. Geophys. Eng. 4, 378–383.
- Shapiro, S.A., Dinske, C., 2009a. Fluid-induced seismicity: pressure diffusion and hydraulic fracturing. Geophys. Prospect. 57, 301–310.
- Shapiro, S.A., Dinske, C., 2009b. Scaling of seismicity induced by nonlinear fluid–rock interaction. J. Geophys. Res. 114, B09307, <http://dx.doi.org/10.1029/2008JB006145>.
- Shapiro, S.A., Royer, J.J., Audigane, P., 1998. Estimating the permeability from fluid-injection induced seismic emission. In: Thimus, J.-F., Abousleiman, Y., Cheng, A.H.-D., Coussy, O., Detournay, E. (Eds.), Poromechanics. Balkema, Rotterdam, pp. 301–305.
- Taron, J., Elsworth, D., 2009. Thermal–hydrologic–mechanical–chemical processes in the evolution of engineered geothermal reservoirs. Int. J. Rock Mech. Min. Sci., <http://dx.doi.org/10.1016/j.ijrmms.2009.01.007>.
- Taron, J., Elsworth, D., Min, K.B., 2009. Numerical simulation of thermal–hydrologic–mechanical–chemical processes in deformable, fractured porous media. Int. J. Rock Mech. Min. Sci. 46 (5), 842–854.
- Xu, T., Pruess, K., 2001. Modeling multiphase non-isothermal fluid flow and reactive geochemical transport in variably saturated fractured rocks: 1. Methodology. Amer. J. Sci. 301, 16–33.
- Xu, T., Pruess, K., 2004. Numerical simulation of injectivity effects of mineral scaling and clay swelling in a fractured geothermal reservoir. Lawrence Berkeley National Laboratory. Paper LBNL-55113.
- Zoback, M., Harjes, H.P., 1997. Injection induced earthquakes and the crustal stress at 9 km depth at the KTB deep drilling site, Germany. J. Geophys. Res. 102, 18477–18492.